Cool Gaseous Exoplanets: surveying the new frontier with Twinkle

Luke Booth [●],[1][★] Subhajit Sarkar [●],[1] Matt Griffin[1] and Billy Edwards [●][2]

[1]*Cardiff Hub for Astrophysics Research and Technology (CHART), School of Physics and Astronomy, Cardiff University, 5 The Parade, CF24 3AA, United Kingdom*
[2]*SRON, Netherlands Institute for Space Research, Niels Bohrweg 4, NL-2333 CA, Leiden, The Netherlands*

ABSTRACT
Cool gaseous exoplanets ($1.75\,R_{\oplus} < R_{p} < 3\,R_{J}$, $200\,\text{K} < T_{eq} < 1000\,\text{K}$) are an as-yet understudied population, with great potential to expand our understanding of planetary atmospheres and formation mechanisms. In this paper, we outline the basis for a homogeneous survey of cool gaseous planets with *Twinkle*, a 0.45-m diameter space telescope with simultaneous spectral coverage from 0.5–4.5 μm, set to launch in 2025. We find that *Twinkle* has the potential to characterise the atmospheres of 36 known cool gaseous exoplanets (11 sub-Neptunian, 11 Neptunian, 14 Jovian) at an SNR $\geq$ 5 during its 3-yr primary mission, with the capability of detecting most major molecules predicted by equilibrium chemistry to $>5\sigma$ significance. We find that an injected mass–metallicity trend is well recovered, demonstrating *Twinkle*'s ability to elucidate this fundamental relationship into the cool regime. We also find that *Twinkle* will be able to detect cloud layers at 3σ or greater in all cool gaseous planets for clouds at $\leq 10\,\text{Pa}$ pressure level, but will be insensitive to clouds deeper than $10^{4}\,\text{Pa}$ in all cases. With these results, we demonstrate the capability of the *Twinkle* mission to greatly expand the current knowledge of cool gaseous planets, enabling key insights and constraints to be obtained for this poorly charted region of exoplanet parameter space.

Key words: instrumentation: spectrographs – techniques: spectroscopic – exoplanets – planets and satellites: atmospheres – planets and satellites: gaseous planets.

1 INTRODUCTION

Over the past three decades, the field of exoplanet science has progressed rapidly, from the first detections in the 1990s (Wolszczan 2012; Mayor & Queloz 1995) and the first atmospheric spectrum in 2002 (Charbonneau et al. 2002), to the revolution in exoplanet demographics resulting from *Kepler* (Lissauer, Dawson & Tremaine 2014; Fulton et al. 2017) and over a decade of transmission spectra from the *Hubble Space Telescope* (*HST*) (Edwards et al. 2022). Most recently, JWST is now returning high precision transmission spectra, resulting in new discoveries such as the first detection of sulphur-bearing species in an atmosphere (Rustamkulov et al. 2023; Alderson et al. 2023; Tsai et al. 2023) and the first detection of carbon-bearing molecules in a habitable zone planet (Madhusudhan et al. 2023). Today over 5500[1] confirmed exoplanets are known, the majority of which have been detected by transit photometry using large dedicated space-based surveys such as *Kepler*, K2, *CHEOPS*, and *TESS*, or ground-based surveys such as WASP, HATNet, and NGTS. Such transiting planets provide potential targets for atmospheric characterization through transmission and/or eclipse spectroscopy. Using these techniques, in the next decade, the upcoming Ariel and

Twinkle missions will perform the first dedicated population-level surveys of exoplanet atmospheres (Tinetti et al. 2018; Edwards et al. 2019a).

The currently known transiting exoplanet population is highly diverse in both radius and temperature, containing planets with radii that vary from less than that of Mercury to several times the size of Jupiter and equilibrium temperatures, T_{eq}, that span the range from less than 200 to over 4000 K. Selection effects of the two most prolific detection methods (transit and radial velocity) bias the currently discovered planetary population towards shorter period planets. Super-Earths and sub-Neptunes are the most frequent type of planet, often found in closely packed multiplanet systems, e.g. the TRAPPIST-1 (Gillon et al. 2017), Kepler-296 (Barclay et al. 2015), Kepler-32 (Swift et al. 2013), and K2-384 (Christiansen et al. 2022) systems. A large population of 'hot Jupiters' is also known, their large size, short periods, and high transit probabilities positively biasing their transit detectability. Notably, some planet populations appear more sparse. These include the 'hot Neptune desert' (Szabó & Kiss 2011; Mazeh, Holczer & Faigler 2016; Edwards et al. 2023) as well as colder gas giants. Wittenmyer et al. (2020), relying on long-duration radial velocity data, determined that the occurrence rates of giant planets around solar-type stars was fairly constant below 300 d and was increased at longer periods. The occurrence rates of hot Jupiters and temperate gas giants would thus be similar ($\sim$1 per cent) but very cold giants, analogous to Jupiter or Saturn, are more frequent ($\sim$7 per cent). Despite this, in practice there is a dearth of known transiting gas giants at cooler temperatures, with about half as many

[1]NASA Archive Planetary Systems Composite Table https://exoplanetarchive.ipac.caltech.edu/cgi-bin/TblView/nph-tblView?app=ExoTbls&config = PSCompPars (2023/09/27)

transiting giants having T_{eq} less than 1000 K as those with T_{eq} greater than 1000 K (around all types of star) (Table 1).

To date, only a small fraction of all known transiting exoplanets, ~ 180 planets[2], have had their atmospheres characterized through a combination of transmission, emission, cross-correlation, and direct imaging spectroscopy, with specific molecular detections reported in about half these cases[3]. The most successful method applied to date has been transmission spectroscopy. This technique is most sensitive to high scale height atmospheres and large planetary radii which tend to augment spectral feature amplitudes. The amplitude of spectral features in transmission A_p can be approximated by:

$$A_p = \frac{2R_p \cdot nH}{R_s^2} \qquad (1)$$

where R_p is the radius of the planet, R_s is the radius of the host star, and H is the pressure scale height. n is commonly taken to have a value of 5, and gives the number of scale heights of a typical spectral features. The scale height is given by:

$$H = \frac{k_B T_{eq}}{\mu g} \qquad (2)$$

where μ is the mean molecular weight of the atmosphere, commonly taken to be ~ 2.3 for hydrogen/helium-dominated (H_2–He) atmospheres, g is the surface gravity of the planet, k_B is Boltzmann's constant, and T_{eq} is the equilibrium temperature of the planet. As well as making the best targets for transmission spectroscopy, large, very hot planets also make better targets for day-side emission spectroscopy due to their higher thermal flux. As a result, currently almost two thirds of all planets that have had their atmospheres analysed have $T_{eq} > 1000$ K, with this population accounting for ~ 70 per cent of planets that have molecular detections[3].

Early searches for trends in exoplanet atmospheres (Sing et al. 2016; Tsiaras et al. 2018; Edwards et al. 2022) have also typically been dominated by hot Jupiters and warm Neptunes. Trends reported include temperature versus cloud/hazes (Crossfield & Kreidberg 2017; Libby-Roberts et al. 2020; Guilluy et al. 2021; Estrela, Swain & Roudier 2022) and planet mass versus metallicity (e.g. Wakeford et al. 2018; Welbanks et al. 2019). Colour–magnitude diagrams and trends regarding phase-curve properties and day–night temperature variations with equilibrium temperature have also been reported (e.g. Zhang 2020). Such population level studies are a start to understanding how atmospheric properties and planet composition relate to fundamental initial conditions, and are key to a full understanding of planet formation and evolution. However, the lower temperature planets are poorly represented due to a paucity of atmospheric spectra in this regime. This in turn is due to a combination of few strong candidates for spectroscopic follow-up and the intrinsic challenge in obtaining transmission spectra for cooler atmospheres (which will have smaller scale heights) at sufficient signal-to-noise ratio (SNR).

In this paper, we examine the capability of the upcoming *Twinkle* space mission to advance the understanding of gaseous planets in the 'cool' regime (which we define as being between 200 and 1000 K), through a dedicated spectroscopic survey consisting of a statistically meaningful sample of such planets. The sample will cover a wide range of temperatures, and include planet sizes ranging from sub-Neptunes to Jovian planets. *Twinkle* will obtain transmission spectra

in the 0.5–4.5 μm wavelength range. Such a survey would have the potential to verify and extend trends into the cool regime, providing key observational constraints for for atmospheric models and planet formation theories.

The paper is structured as follows: Section 2 outlines the scientific case for studying cool gaseous exoplanets, which is followed by a brief description of the *Twinkle Space Telescope* in Section 3. Section 4 describes the construction of a preliminary candidate list based on known exoplanets spanning the parameter space of the cool gaseous planet population. Sections 5 and 6 describe two simulated studies performed on planets from the preliminary candidate list. Section 5 explores the ability of *Twinkle* to constrain atmospheric metallicity and recover an injected metallicity trend, whilst Section 6 examines *Twinkle*'s sensitivity to detecting clouds in gaseous planets over a range of sizes and temperatures.

2 COOL GASEOUS PLANETS

Spectroscopic observations of 'cool' gaseous planets provide the opportunity to shed light on the physical and chemical processes that govern H_2–He dominated atmospheres at low temperatures and the formation histories of this population.

2.1 Categorization

In this paper, we sub-categorize the cool gaseous planets into nine sub-groups based on size and temperature. A survey of cool gaseous planets across the full parameter space of size and temperature will allow the possibility of trends to be elucidated with respect to both parameters. We limit the lower bound of temperature we consider to 200 K. Below this level, the temperatures are generally beyond the outer limits of the 'habitable zone', corresponding closer to those of the cold gas and ice giants of our Solar System and in practice, there are hardly any transiting planets below this lower limit. Our upper temperature bound is 1000 K, which previous studies have used to define as boundary between hot Jupiters and cool giants (Thorngren, Marley & Fortney 2019; Wallack et al. 2019). Avoiding terms like 'temperate' or 'warm' which have no consensus definitions, we call all planets in this temperature range 'cool'. We choose to further sub-divide the large cool temperature regime into three distinct temperature brackets: C1 (200–500 K), C2 (500–750 K) and C3 (750–1000 K) as distinctive patterns of chemical and physical processes are likely to occur with temperature. The C1 category would encompass planets in the 'habitable zone'. In terms of size, we include established planetary classes with radii above the Kepler radius valley mid-point ($1.75 R_\oplus$): sub-Neptunes ($1.75 R_\oplus$–$3 R_\oplus$), Neptunes ($3 R_\oplus$–$0.5 R_J$) and Jovians ($0.5 R_J$–$3 R_J$). These are planets where primary H_2–He dominated atmospheres are likely to be the norm (Fulton et al. 2017; Gupta & Schlichting 2019). Their low-mean molecular weights will mitigate some of the challenges associated with observing cool atmospheres, and hence they are favoured over rocky planets in this temperature regime for transmission spectroscopy.

2.2 The workings of cool atmospheres

In the low-temperature regime, we would expect molecules such as NH_3 and CH_4 to dominate over N_2, CO_2, and CO in thermochemical equilibrium, with final abundances modulated by bulk elemental composition (higher metallicities tend to favour CO and particularly CO_2 over CH_4 and N_2 over NH_3) or the C/O ratio (Madhusudhan 2012; Moses 2014). However, at lower temperatures reaction rates

---

[2]ExoAtmospheres community data base (2023/11/13) http://research.iac.es/proyecto/exoatmospheres/index.php

[3]Defined as where one or more molecules have definitive detections reported in the ExoAtmospheres community data base, but excluding cases where only upper limits are given.

slow, such that the time-scale for reaching chemical equilibrium increases compared to hotter atmospheres. Competing disequilibrium processes such as transport processes (e.g convection and eddy diffusion) and photochemistry would be expected to have stronger effects than in hotter atmospheres (Prinn & Barshay 1977; Zahnle & Marley 2014). Molecules that tend to occur at low temperatures, like CH_4 and NH_3, are also more sensitive to photochemistry than their hot counterparts (CO and N_2) (Moses 2014). Such processes can change the composition, radiative balance and temperature–pressure profiles (Moses 2014). HCN may be a significant molecule in cooler atmospheres as a result of coupled NH_3–CH_4 photochemistry, and CO may occur in the IR photosphere through CH_4–H_2O photochemistry or transport-induced quenching, but always at lower abundances than CH_4 (Moses 2014).

The quench level is the atmospheric level where the chemical equilibrium time-scale for a given reaction just falls below that for vertical (or horizontal) mixing, and the molecular abundances at this level are then transported to higher altitudes, resulting in a complex disequilibrium composition (also modulated by photochemistry) in the upper layers potentially probed in transmission. In these upper layers, photochemical time-scales may be expected to be shorter than chemical equilibrium, so we might expect to see the byproducts of photochemistry at greater levels than for hotter atmospheres. From breakdown of the photosensitive molecules CH_4 and NH_3, complex hydrocarbons and nitriles are more likely to occur in colder than in hotter atmospheres (Moses 2014). This could include high-altitude photochemically produced hazes which may modulate the energy balance of the planet. Photochemical reactions can also result in species that cause atmospheric warming and inversions or conversely could act as coolants (e.g. cooling by C_2H_2 and C_2H_6, byproducts of methane photolysis in the atmosphere of Jupiter). Cloud condensates may form, reflecting the condensation profiles of low-temperature molecules, giving rise to water, methane, or ammonia clouds, which will also impact albedo and energy balance. The presence of clouds will also impact the measured quantities of the condensed species at higher altitudes reflected in the spectrum. The exact mechanisms and chemical pathways for disequilibrium chemistry remain an area of active research, as highlighted by the detection and subsequent interpretation of SO_2 in the atmosphere of the hot Saturn WASP-39 b by the JWST Early Release Science (ERS) team (Tsai et al. 2023; Rustamkulov et al. 2023; Alderson et al. 2023). Therefore, while disequilibrium processes are expected and sophisticated atmospheric models exist to simulate the transport-induced quenching (e.g Moses et al. 2011; Drummond et al. 2020; Zamyatina et al. 2023) and photochemistry (e.g. Tsai et al. 2017), there are few if any observational constraints on the chemical kinetics from exoplanet observations. Further to this, there is a present lack of data on how planet and therefore gaseous envelope size would affect these processes. A large and diverse spectroscopic survey of cool gaseous planets is ideally placed to find such 'smoking guns'.

2.3 Planet formation quandaries

Clues to the formation history of an exoplanet are encoded in its composition and therefore its atmospheric spectrum. Elemental ratios, such as the C/O ratio, may be able to locate a planet origin location relative to different 'ice lines' in the protoplanetary disc (e.g. Öberg, Murray-Clay & Bergin 2011) and could be measurable in an exoplanet atmosphere. The C/O ratio may be complicated by planet migration and/or planetesimal pollution. It may be possible to disentangle such pollution effects from origin location effects by examining a range of element ratios (e.g. Turrini et al. 2021;

Pacetti et al. 2022). Measurement of the atmospheric metallicity may also provide evidence for the formation mechanism. In core-accretion scenarios, the atmospheric metallicity is expected to be increased compared to the host star (Thorngren et al. 2016), whereas in gravitational instability scenarios, we would expect a near stellar metallicity. Current characterizations of the mass–metallicity relationship (e.g Wakeford et al. 2018; Welbanks et al. 2019) are supportive of core-accretion, but have large uncertainties and are derived mostly from hot giant exoplanets. Theoretical structural evolution models (Thorngren, Marley & Fortney 2019) indicate that the mass–metallicity trend should continue in planets <1000 K; however, there is currently limited data to test and confirm this.

Cool gaseous planets may present a challenge to planet formation theories. To hold onto an H_2–He atmosphere requires the rapid formation of a massive core $\geq 10\,M_\oplus$ (e.g. Pollack et al. 1996). Traditional core accretion theory holds that such cores are more likely to form beyond the ice line where water ice adds to bulk and adhesion. However, many gaseous planets ranging from sub-Neptunes, through Neptune-sizes to Jupiter-sizes are found with equilibrium temperatures that would put them within the ice line. Indeed Hill et al. (2018) found >70 planets of size $>3\,R_\oplus$ in the habitable zones of G, K, and M-type stars, with occurrence rates ranging from 6 to 11.5 per cent depending on the stellar class. A planet formation quandary therefore exists in explaining the formation of these planets, requiring some modifications to basic core accretion models. Another problem is the presence of gas giants around M-dwarf stars (many of which are in the cool regime) (e.g. Kanodia et al. 2023), where core accretion models predict slower accretion rates (e.g. Ida & Lin 2005; Burn et al. 2021) that would make large core formation challenging on the time-scale of the disc lifetime. Gravitational stability is also a potential pathway to forming giant exoplanets (Boss 1997) and has seen renewed interest due to its ability to explain the existence of the growing number of M-dwarf gas giant exoplanets. For gaseous planets within the water ice-line, formation scenarios include core-accretion beyond the water-ice line followed by disc-migration (Paardekooper & Johansen 2018), or core formation interior to the water-ice line, followed by *in situ* enrichment via gas, dust, and pebble accretion close to the host star (Knierim, Shibata & Helled 2022), along with other variations of the above models proposed in recent years.

Compositional information including atmospheric metallicity and elemental ratios such as the carbon-to-oxygen ratio (C/O) may therefore shed light on planetary formation and evolution processes in this regime.

2.4 Moons and habitability

Giant planets have long been postulated to be likely exomoon hosts (Heller & Pudritz 2015; Spalding, Batygin & Adams 2016; Saillenfest et al. 2023), and although multiple exomoon candidates have been identified, there has yet to be a definitive detection (Sucerquia et al. 2020; Rovira-Navarro et al. 2021; Kipping & Yahalomi 2023). Though moons can form around planets of any size, cool gaseous planets may have a higher probability of hosting exomoons, owing to their having probably migrated inwards a shorter distance than hotter planets of a similar size and therefore being less likely to have undergone disruption the orbits of, or ejection of, their moons (Spalding, Batygin & Adams 2016). Furthermore, if such moons are sufficiently large, they themselves may have atmospheres, generated through mass transfer from their parent planet or, more likely, outgassing or volcanism as a result of tidal heating. Transmission spectroscopy may therefore provide a method by which exomoons

could be detected around cool gaseous planets, with typical products of volcanism (including sodium- and potassium-bearing species) (Rovira-Navarro et al. 2021) unlikely to feature in cooler gaseous atmospheres. Thus cool giant spectroscopy may potentially yield evidence for the presence of exomoons. However, investigating this fascinating possibility requires a determination of the abundance of potential volcanic tracers and subsequently their detection feasibility with current and future instrumentation (eg: *Twinkle*, *Ariel*, JWST, and ELTs). This is beyond the scope of the current paper and is left to future work. We also note that such exomoons could be in the habitable zone in some cases, and therefore could be locations for potential habitability. The habitability of cold giants themselves is an unexplored topic, and while liquid water layers or oceans such as those postulated for Hycean sub-Neptunes (Madhusudhan, Piette & Constantinou 2021) can be ruled out on the basis of pressure and temperature, the possibility of aerial biospheres could be explored. This has previously been raised in the context of Jupiter (Sagan & Salpeter 1976), and more recently in brown dwarfs (Yates et al. 2017; Lingam & Loeb 2019), sub-Neptunes (Seager et al. 2021) and Venus (Greaves et al. 2021).

2.5 Previous observations

Relatively few cool gaseous planets have been studied spectroscopically to date. Sub-Neptunes are ubiquitous but small in size (reducing the A_p factor in equation 1), so despite the large number, there are few targets suitable for spectroscopic follow-up. None the less, several sub-Neptunes in the 'cool' regime have been studied spectroscopically. A non-exhaustive list includes: K2-18 b (Tsiaras et al. 2019; Benneke et al. 2019b; Bézard, Charnay & Blain 2020; Madhusudhan et al. 2023), GJ 1214 b (Kreidberg et al. 2014; Gao et al. 2023; Kempton et al. 2023), GJ 9827 d (Roy et al. 2023), HD 3167 c (Guilluy et al. 2021), HD 97658 b (Knutson et al. 2014b), and TOI-270 d (Mikal-Evans et al. 2023). Spectra of these planets have revealed greatly contrasting atmospheres. Observations conducted by *HST*, and more recently JWST, have shown the spectrum of GJ 1214 b to be flat well into the mid-infrared (Kreidberg et al. 2014; Gao et al. 2023), requiring significant cloud / haze production to explain, whilst *HST* spectra of K2-18 b showed clear absorption features at 1.4 μm relatively unimpeded by the presence of cloud.

This feature has been inferred to be due to the presence of H_2O (Tsiaras et al. 2019; Benneke et al. 2019b) or CH_4 (Bézard, Charnay & Blain 2020; Blain, Charnay & Bézard 2021), with recent JWST/NIRISS and NIRSpec observations strongly detecting CH_4 (Madhusudhan et al. 2023). Absorption features at ~1.4 μm, interpreted as due to H_2O have also been seen in *HST* spectra of GJ 9827 d, HD 3167 c, and TOI-270 d, though observations spanning broader wavelengths are required to fully resolve the known degeneracy between H_2O and CH_4.

Neptune to Jupiter-sized giant planets in the cool regime are also poorly characterized spectroscopically. In terms of temperature, such planets provide a 'missing link' between the two well-studied planetary populations of hot Jupiter exoplanets and the giants of our own Solar System. Previous spectra of such planets include those for GJ 436 b (Knutson et al. 2014a; Hu, Seager & Yung 2015), GJ 3470 b (Benneke et al. 2019a), HD 106315 c (Guilluy et al. 2021; Kreidberg et al. 2022), HIP 41378 f (Alam et al. 2022), Kepler-51 b, d (Libby-Roberts et al. 2020), K2-33 b (Thao et al. 2023), WASP-29 b (Wong et al. 2022), WASP-80 b (Bell et al. 2023a), and WASP-107 b (Kreidberg et al. 2018; Spake, Oklopčić & Hillenbrand 2021), though many additional planets in this size regime have been

the target of ground-based searches for metastable helium absorption (Vissapragada et al. 2022; Allart et al. 2023).

Despite the increased number of spectra in the cool giant regime, these atmospheres remain poorly understood. Multiple planets, including HIP-41378 f, Kepler-51 b, d, K2-33 b, and WASP-29 b, exhibit spectra that are flat and featureless across the *HST*/WFC3 wavelength range, while others exhibit clear or muted absorption features at ~1.4 μm.

2.6 Surveys of cool gaseous planets

There is a scarcity of systematic surveys of cool gaseous planets with high precision spectra. Kammer et al. (2015) obtained *Spitzer* secondary eclipse measurements at 3.6 and 4.5 μm for five gas giants in the temperature range 980–1184 K. They used the atmospheric CH_4/CO ratio as a marker of atmospheric metallicity, with results somewhat supportive of increased metallicity with lower masses. Wallack et al. (2019) performed a similar *Spitzer* study on five further gas giants with $T_{eq} < 1000$ K. They found no evidence for a Solar-System-like mass–metallicity relationship but did find a relationship between inferred $CH_4/(CO + CO_2)$ and stellar metallicity. More recently, Baxter et al. (2021) performed transmission photometry of 33 gaseous planets at 3.6 and 4.5 μm using *Spitzer*, of which 13 had temperatures between 500 and 1000 K. There was some evidence of a mass–metallicity relation: the cool planets (<1000 K) were generally biased with lower mass and appeared to have higher metallicity as well as lower eddy diffusion coefficients and a lack of methane compared to expectations. A lack of methane had previously been noted on a number of cool planets comparedmean to equilibrium expectations constituting the so-called 'missing methane problem'. Methane has now recently been detected in two 'cool' gaseous planets with JWST: K2-18 b and WASP-80 b (Madhusudhan et al. 2023; Bell et al. 2023a). More recently a Cycle 2 JWST survey of seven giant planets in the 'cool' regime orbiting M-dwarf stars has been planned (JWST Proposal 3171, PI: S. Kanodia).

There is therefore a need for a homogeneous cool gaseous planet survey with wide wavelength coverage to further explore and constrain the relationship between planet mass and atmospheric metallicity, and open up this field of study. Cooler gaseous planets may provide more robust metallicity measurements than hotter gaseous planets as they will be significantly less affected by the degeneracy in radius between poorly understood radius inflationary effects and increasing metallicity (and thus mean molecular weight) which acts to suppress the atmospheric extent (Thorngren et al. 2016). Improved metallicity measurements may also help to validate and extend reported mass–metallicity trends (Wakeford et al. 2018; Welbanks et al. 2019) or support the absence of a trend (Edwards et al. 2022). Furthermore, the temperature range spanned by cool gaseous planets is likely to aid in the exploration of cloud and haze coverage trends predicted from theoretical and laboratory work, hints of which have been seen in early *HST* observations (Dymont et al. 2022; Estrela, Swain & Roudier 2022; McGruder et al. 2023).

Whilst the number of known cool giant planets is comparatively small, it has been steadily growing. In the last 18 months alone, *TESS* photometry has led to the discovery of intriguing cool giants such as the low-density warm-Jovian TOI-1420 b (Yoshida et al. 2023), a warm Saturn TOI-199 b (Hobson et al. 2023), and several around M-dwarf stars (e.g. Powers et al. 2023; Harris et al. 2023; Han et al. 2023). Re-observation of *TESS* sectors during the second extended mission has enabled single transit and 'duotransit' planetary candidates (Hawthorn et al. 2023), many with orbital periods longer than ~15 d, to be confirmed, with follow-up efforts by ground-

based surveys such as the *Next Generation Transit Survey* (NGTS) and the *CHEOPS* space telescope subsequently hunting down and constraining the true orbital periods of these candidates. Examples of 'cool' planets found in this manner include the sub-Neptunes HD 22946 d (Garai et al. 2023) and HD 15906 b and c (Tuson et al. 2023), the Neptunes HD 9618 b and c (Osborn et al. 2023), TOI-5678 b (Ulmer-Moll et al. 2023) and the Jupiters TOI-4600 b and c (Mireles et al. 2023) (planet c having a T_{eq} of 191 K).

However, compared to planets with hot atmospheres, cooler gaseous planets will have smaller scale heights and thus spectral features will give lower SNRs. Co-adding of multiple transit observations is frequently used to improve SNR, but increases total observing time required. This is even more problematic for planets orbiting Sun-like stars where orbital distances are greater and periods longer. As such, it is observationally more intensive to characterize cool gaseous planets (especially around Sun-like stars), and this is one reason why they are a challenging population. Dedicated spectroscopic surveys permitting repeat observations over several years would be key to opening up this population to detailed characterization and obtaining sufficient homogenized samples for population-level studies. Two such dedicated surveys are planned in the coming decade: the ESA Ariel mission due for launch in 2029 and the *Twinkle* mission which will precede it with a planned launch in 2025.

3 TWINKLE

Developed commercially by Blue Skies Space Ltd. (BSSL), *Twinkle* is a fast-tracked satellite based on heritage components, and that is expected to characterize many exoplanetary and Solar System targets during its nominal 7-yr lifetime (Edwards et al. 2019a; Stotesbury et al. 2022). Expected to launch in late 2025, the spacecraft will carry a 0.45-m diameter primary mirror, with an inner sanctum that is actively cooled to <90 K. *Twinkle* has a spectrometer with two simultaneously operating channels across the visible and infrared: CH0 covering 0.5–2.4 µm at R ≤ 70 and CH1 covering 2.4–4.5 µm at R ≤ 50, each channel having its own grism element (Stotesbury et al. 2022). *Twinkle* will therefore expand on the total spectral wavelength coverage of *HST* WFC3 G102 (0.8–1.15 µm) and G141 (1.075–1.7 µm) gratings by a factor of ~5, whilst retaining similar spectral resolution. This will open up the opportunity to potentially break degeneracies between H_2O and CH_4 that are known to exist in WFC3 observations, whilst also enabling the detection of strong absorption features from molecules such as CO_2 (2.0, 2.7, 4.3 µm), CO (2.34, 4.67 µm), and NH_3 (1.5, 2.0, 2.3, 3.0 µm) which lie outside the wavelength range covered by WFC3.

Twinkle has a field of regard centred on the anti-Sun vector encompassing ±40° about the ecliptic (Edwards et al. 2019a). The primary exoplanet survey mission will take place in the first 3 yr of operation. *Twinkle* will therefore be uniquely positioned to provide homogeneous spectroscopic characterization of a large number of exoplanetary atmospheres, something that will be challenging to achieve with JWST due to competition with other astrophysical disciplines for valuable telescope time.

Launching several years prior to the European Space Agency's M4 mission, *Ariel*, which has a 1-m class primary mirror and wavelength coverage from 0.5–7.8 µm (Tinetti et al. 2018), *Twinkle* will additionally act as a useful precursor, observing many targets that fall within the current realisation of the Ariel target list over a substantially shared region of wavelength space. Consequently, insights gained from *Twinkle* may be useful for informing future iterations of the *Ariel* target list, allowing the combined science output of the two missions to be optimized.

With the capability to provide the first large homogeneous survey of exoplanet atmospheres, we seek to explore *Twinkle*'s ability to identify key molecules and elucidate trends in a population level study of cool gaseous planets, which we propose to integrate into the science plan of the *Twinkle* Extrasolar Survey (Twinkle collaboration in preparation).

4 ESTABLISHING A CANDIDATE LIST FOR THE *TWINKLE* COOL GASEOUS PLANET SURVEY

Candidate list construction for the proposed *Twinkle* cool gaseous planet survey uses the data base of confirmed planets from the NASA Exoplanet Archive[4] to establish a preliminary target list of known planets. Transiting planets are selected based on three criteria:

1) the existence of 'transit' listed as the discovery method;
2) the presence of a non-zero transit depth;
3) the presence of a transit duration value,

with any planet not meeting one or more of these criteria being filtered out. Planets with radii <1.75 $R_\oplus$ are also removed, resulting in a list of transiting sub-Neptunian, Neptunian and Jovian class planets (see Table 1). To obtain the sample observable with *Twinkle*, we perform a cut that eliminates planets with host stars outside ±40° of the ecliptic. The remaining 383 planets with radii between 1.75 $R_\oplus$ and 3 R_J and T_{eq} between 200 to 1000 K form an initial *Twinkle* cool gaseous planet candidate list. The candidate list will be modified prior to launch as new discoveries are made.

The initial candidate list is subjected to an SNR study, used to identify the number of transits required for each planet to achieve atmospheric detectability with *Twinkle*. The findings of this study are then used to further filter the candidate list, leaving only planets that can be observed at or above the target SNR threshold during *Twinkle*'s mission lifetime. This includes a cautious estimate of *Twinkle*'s observing efficiency, scaling up the number of transits required to meet the SNR threshold by a uniform factor for each planet and resulting in our final lists of suitable and preferred candidates for the primary 3-yr and extended 7-yr *Twinkle* exoplanet surveys.

4.1 Establishing candidate planet SNR

Before examining the number of transits needed for each planet, we need to decide on a threshold SNR for spectral feature detection where the SNR is the ratio of the amplitude of a typical spectral feature A_p to the noise on the transit depth (1σ error bar) $\sigma_p(\lambda)$ at a given spectral binning. If we assume a typical spectral feature corresponds to 5 scale heights, then we can use equation (1) to find A_p with $n = 5$, and H for a given planet is obtained from equation (2). The error bar for a given target SNR is given by

$$|\text{error bar}| = \frac{2 \cdot 5 \cdot H \cdot R_p}{R_s^2} \cdot \frac{1}{\text{SNR}_{\text{target}}} \quad (3)$$

We wished to verify that SNRs calculated this way corresponded to detectability of prominent molecules at high significance when simulated using an atmospheric radiative transfer code with parameters retrieved via Bayesian parameter estimation ('spectral retrieval'). The latter reflects the method of analysis that would be applied to a real observed transmission spectrum. We decided to investigate nominal SNRs of 3 and 5. To this end, a subset of the *Twinkle*

[4]Planetary Systems Composite Table accessed 2022/07/22

Table 1. Population statistics for transiting exoplanets [derived from NASA Exoplanet Archive Planetary Systems Composite Table accessed 2022/07/22]. Total numbers are shown in black, and the corresponding numbers of cool gaseous planets accessible within the field-of-regard (FOR) of the *Twinkle* space telescope are shown bracketed in grey. The equilibrium temperatures for this table were obtained from the NASA archive where available or otherwise calculated from stellar and orbital parameters (assuming an albedo of 0.3). At the time of submission, the number of cool gaseous planets in the *Twinkle* FOR had increased from the 383 shown to 416.

		Sub-Neptunian ($1.75\,R_\oplus \leq R_p < 3\,R_\oplus$)	Neptunian ($3\,R_\oplus \leq R_p < 0.5\,R_J$)	Jovian ($0.5\,R_J \leq R_p < 3\,R_J$)
Hot	($T_{eq} \geq 1000\,K$)	222	78	499
C3	($750 < T_{eq} < 1000\,K$)	388 (75)	117 (30)	84 (40)
C2	($500 < T_{eq} \leq 750\,K$)	528 (109)	166 (32)	54 (22)
C1	($200 < T_{eq} \leq 500\,K$)	309 (59)	118 (7)	75 (9)
Cold	($T_{eq} \leq 200\,K$)	1	3	6

Table 2. Detection significances (in σ) of H_2O and CO obtained from retrievals conducted on simulated atmospheres for eight planets spanning the cool gaseous planets parameter space. Detection significance of CH_4 is $>5\sigma$ in all cases.

| Planet name	Detection significance of individual molecules			
	Water (H_2O)		Carbon monoxide (CO)	
	SNR $\geq$ 3	SNR $\geq$ 5	SNR $\geq$ 3	SNR $\geq$ 5
WASP-11 b	4.4	>5.0	1.8	1.7
HD 63935 b	>5.0	>5.0	1.7	1.7
HD 106315 c	>5.0	>5.0	1.8	1.3
TOI-1130 c	3.5	>5.0	1.8	1.7
GJ 436 b	4.2	>5.0	1.7	1.9
HD 136352 c	4.5	>5.0	1.6	2.0
AU Mic c	3.1	5.0	1.8	1.9
TOI-178 g	4.3	>5.0	2.0	2.0

Figure 1. Modelled VMRs for HD 106315 c. Solid lines denote altitude-dependent chemical profiles under equilibrium conditions, whilst dashed vertical lines denote profile-averaged VMRs.

cool gaseous candidates (listed in Table 2) have their atmospheres simulated using TauREx3 (hereafter TauREx) (Waldmann et al. 2015; Al-Refaie et al. 2021) as described further below. For a given planet, in the calculation of H, T_{eq} and g are obtained and derived respectively from system values used by the *Twinkle* radiometric tool, *TwinkleRad* (Stotesbury et al. 2022), based on *ExoRad* (Mugnai et al. 2022), whilst μ is obtained directly from the TauREx atmospheric model. This allows calculation of A_p for each planet, and error bars for SNRs of 3 and 5 obtained using equation (3).

For each planet, the atmospheric model and resulting model transmission spectrum are obtained as follows. TauREx was run initially using a model with 100 plane-parallel atmospheric layers spanning pressures from 10^{-6} to 10^5 Pa, an isothermal temperature–pressure (T–P) profile at equilibrium temperature, T_{eq}, and equilibrium chemistry set by the taurex_ace plugin based on the ACE equilibrium chemistry regime of Agúndez et al. (2012, 2020), generated using solar C/O-ratio and metallicity values obtained for each planet using the trend found in Welbanks et al. (2019). Altitude-dependent volume mixing ratios (VMRs) obtained this way for each molecule were then simplified to a single VMR value by taking the average across the profile (Fig. 1) with this single value subsequently being used to set the free chemistry in the final model. The model was thus run again with the same initial conditions except this time with free chemistry, i.e. the fixed VMRs for the most abundant molecules (VMR $> 10^{-8}$), to give a final transmission spectrum. We use opacity cross-sections from ExoMol (Tennyson & Yurchenko 2016) that include H_2O, CH_4, CO_2, CO, and NH_3. In addition to molecular absorption, contributions from Rayleigh scattering and collision-induced absorption (CIA) between H_2–H_2 and H_2–He were
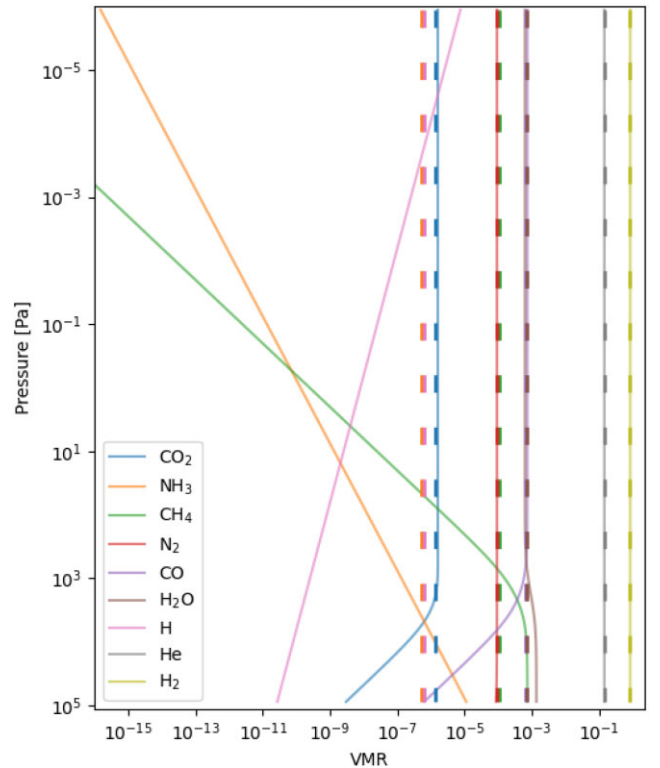
included[5]. To simulate an observed spectrum, the resulting near-local thermal equilibrium (near-LTE) cloud-free atmospheric spectra were then binned across the wavelength range covered by both *Twinkle* spectroscopic channels to a fixed spectral resolution of $R = 50$, approximating the performance of the instrument as detailed above. To these binned points, error bars were then added according to equation (3), for the SNR = 3 and SNR = 5 cases. An example of such a simulated observed spectrum is shown in Fig. 2 together with the different contributions to the spectrum.

---

[5]This work utilizes molecular cross-sections from 0.3–50 μm sampled at R = 15 000, which can be found at https://www.dropbox.com/sh/13y33d02vh56jh2/AACh03L5h1QEbDYN7_-jMjBza/xsec/xsec_sampled_R15000_0.3-50?dl=0&subfolder_nav_tracking = 1. Rayleigh scattering data for all included atmospheric molecules and CIA files from HITRAN 2011 available at the above link are also used.
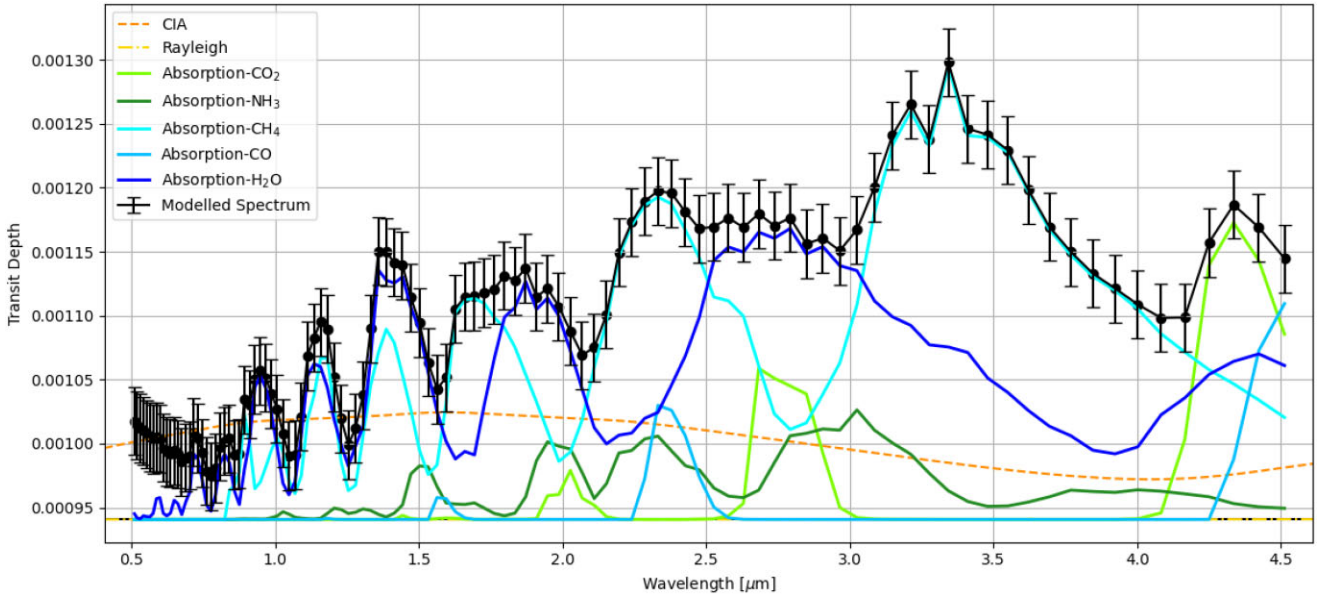
Figure 2. Forward modelled spectrum for candidate HD 106315 c, binned to R = 50 from 0.5–4.5 μm. Molecular absorption components are shown at the binned resolution of the final spectrum. Also shown are the total contributions to the final spectrum from CIA (between H_2–H_2 and H_2–He) and Rayleigh scattering (all atmospheric molecules), with the final spectrum shown in black.

We note here that although disequilibrium chemistry processes and clouds and hazes are expected to be present in sub-1000 K planetary atmospheres (Fortney et al. 2020; Dymont et al. 2022; Fleury et al. 2023), such processes are poorly constrained at present, and hence the extent to which they may impact an individual planet cannot be evaluated with accuracy at this time. We have therefore not attempted to include these processes in the atmospheric models created for this study, which should suffice for the purpose of establishing detectability of general spectral features.

Bayesian spectral retrievals are then conducted on the binned forward-modelled spectra produced using the nested sampling algorithm nestle[6] initiated in 'single' mode with 150 live points. For each planet (with error bars corresponding to SNR = 3 or SNR = 5), the following retrievals are performed. First, a baseline retrieval with the 'full atmospheric' model, containing all atmospheric constituents with VMRs > 10^{-8} (which generally included H_2O, CH_4, CO_2, CO, and NH_3). The remaining three retrieval models are each initiated in the same manner as the full atmospheric model, but without one of either H_2O, CH_4, or CO. We select these molecules as they are found to consistently have the highest VMRs in our forward models. By comparing the Bayesian evidence obtained to that of the full atmospheric model, detection significances could be ascertained for each molecule. The detection significance of the three molecules is obtained via the log Bayes factor (Trotta 2008; Benneke & Seager 2013), which is the difference in the log Bayesian evidence between full atmospheric model and the model with the molecule omitted.

We find that for all the selected planets (Table 2), CH_4 is detected at >5σ in all cases whether the error bars are derived from an SNR of 5 or 3. With SNR = 5, H_2O is detected to ≥5σ in all cases, but at SNR = 3, water detection significance falls to a minimum of ∼3 (Table 2). Our molecular detectability study also reveals that for the eight planets studied, CO is never detected above 2σ, irrespective of SNR. Given the high VMR of this molecule in the forward

models (log[VMR_{CO}] = −3 to −4), we attribute the weakness of detection to two factors. As can be seen in Fig. 2, CO features at shorter wavelengths (∼1.6 and 2.34 μm) are masked by spectral features from CH_4 and H_2O when all three molecules have similar atmospheric abundances, owing to CH_4 and H_2O having larger cross-sections. This challenge in robustly detecting CO is further compounded by the fact that the strongest observable band peaks at 4.7 μm, just beyond the wavelength range covered by *Twinkle* (Edwards et al. 2019a).

Given that when we utliize error bars derived from an assumed SNR of 5, we obtain excellent detection significances for H_2O and CH_4 in all cases studied, we proceed by adopting SNR = 5 as the threshold to attain for all planets in the *Twinkle* initial candidate list.

4.2 Preliminary candidate list

We next take the initial 383 candidates and estimate the number of transits needed in each case to reach an SNR of 5. To calculate SNR, we again find A_p for each planet using equation (1), but this time, we obtain the transit depth errors from the radiometric tool, *TwinkleRad* (Stotesbury et al. 2022) [via B. Edwards private communication]. *TwinkleRad* gives the 1σ error bar values on the transit depth for for a single transit. These values account for photon noise and instrumental effects and assume 100 per cent observing efficiency. The error bars from *TwinkleRad* are given at the 'native' wavelength grid of its *Twinkle* model, which has a median resolving-power of 42 (ranging from 18–70). Model transmission spectra are thus binned to this native grid.

Since the error on the transit depth is in reality wavelength dependent, so is the SNR. However, a single representative value was needed for a given planet for calculation of the number of transits. For this, we use the lower quartile value for SNR across the full wavelength range covered by both channels. This ensures that 75 per cent or more of the spectrum achieves or exceeds the target SNR of the observation and that individual planets are not negatively biased by a single low-impact data point.

[6]https://github.com/kbarbary/nestle

In order to account for loss of data during Earth-occultation events that will arise due *Twinkle*'s low-Earth orbit, we scale the *TwinkleRad* error bars by a factor of $1/\sqrt{0.75}$. This is done to simulate a conservative observing efficiency of 75 per cent, assumed to be the case for all planets within our observing sample. Consequently, we recalculate the representative single transit SNR of each planet, then obtain the number of transits, N_t, required to reach a threshold SNR of 5, rounded up to the nearest integer:

$$N_t = \left(\frac{5}{\text{SNR}_1} \right)^2 \tag{4}$$

where SNR_1 is the lower quartile SNR for a single transit. We combine this information with the orbital period for each planet to compute if the required number of transits could be observed within 3 or 7 yr. This way we obtain a final candidate list of 36 and 57 planets for the primary (3-yr) and extended (7-yr) missions, respectively. We show the distribution in the radius–temperature plane of the 57 candidates in the *Twinkle* 7-yr extended mission list in Fig. 3. The final candidates are further separated into five distinct tiers using the following assigned criteria based on N_t and the total integration time, T_{int}. The latter is calculated assuming a single transit observation lasts $3 \times T_{14}$, where T_{14} is the transit duration. The expectation is that a subset of higher tier candidates will be observed by *Twinkle* during its lifetime.

(i) Tier 1: $N_t < 25$ **and** $T_{\text{int}} \leq 25$ d
(ii) Tier 2: $N_t < 50$
(iii) Tier 3: $N_t < 100$
(iv) Tier 4: $N_t < 150$
(v) Tier 5: any other candidates

The candidates are listed with their N_t, T_{int}, and tierings in Table A1 and Table A2. These planets therefore give the preliminary candidate list for the *Twinkle* cool gaseous survey and for the studies in this paper. We note that 26/36 planets of the 3-yr survey and 46/57 for the 7-yr survey do not have any current transmission spectra. However, since this analysis was completed, the number of cool gaseous targets in the *Twinkle* FOR has increased by 8 per cent (Table 1), and will continue to do so up to the time of the mission. Our sample size thus represents a conservative value, with the final target list likely to be somewhat larger. While it is possible that some of these planets will be observed with JWST prior to the launch of *Twinkle*, the *Twinkle* survey being a homogeneous survey, inclusion of JWST planets in the sample would still be important. We note that large numbers of transits are required for many planets in the sample which may ultimately not be practical in the real mission. However, we expect Tier 1 planets (which range in N_t from 1 to 22 transits) would be practical. Tier 2 planets may also be quite possible. Thus while the full sample shown here may not be ultimately adopted, a significant sub-sample of high-tier planets exists, covering a wide range of size and temperature, which would make a sizeable survey.

5 METALLICITY TREND DETECTION STUDY

One of the key properties for planet characterization is metallicity, which is commonly split into two regimes: *bulk*, describing the heavy-element content of the total planet and *atmospheric*, pertaining to the atmosphere alone. As mentioned previously, atmospheric metallicity and elemental ratios can provide clues to the formation mechanism, location and migration history of the planet. Atmospheric metallicity and elemental ratios, e.g. the C/O ratio, also set the initial elemental mix that controls the abundances of molecular species seen in thermochemical equilibrium. The possible inverse

relationship between planet mass and metallicity is consistent with core accretion scenarios. In this study, we take the *Twinkle* cool gaseous planet preliminary sample and investigate *Twinkle*'s ability to elucidate a mass–metallicity trend in this sample, if one exists.

5.1 Elucidation of a mass–metallicity trend

We explore here whether an injected atmospheric metallicity trend can be recovered from a simulated atmospheric survey of cool gaseous planets using the *Twinkle* 7-yr candidate list (Tables A1 and A2). The candidate list is well suited for this investigation spanning two orders of magnitude in mass.

We construct atmospheric forward models for each planet on the list, using TauREx, binning these to the native *Twinkle* wavelength grid and adding rescaled wavelength-dependent error bars obtained from *TwinkleRad* to the resulting spectrum. The scaling accounts for the assumed observing efficiency of *Twinkle* (75 per cent) and the unique number of transits, N_t, required for each planet in the sample to reach the desired SNR threshold of 5. Our forward models have molecular abundances dictated solely by ACE equilibrium chemistry initialized with C/O = 0.54 (solar) and a unique metallicity value for each planet obtained using the H_2O abundance mass–metallicity trend (including WASP-39 b) of Wakeford et al. (2018). We use this reference since the metallicity values are given in units of solar metallicity, and the retrieved metallicities from TauREx are given in the same units. 10 planets in the sample do not have currently measured masses but their estimated masses given in the NASA Exoplanet Archive are used for this purpose (these are planets for which there are no errors given in Tables A1 and A2).

Model atmospheres are again generated using a simple isothermal T–P profile spanning 100 plane-parallel layers 10^{-6} to 10^5 Pa (10^{-11} bar to 1 bar) and assume cloud-free conditions; however unlike the final models used in Section 4.1, we retain the full, altitude-dependent, VMR profiles for each chemical species. Transmission spectra are then generated from this atmospheric model by including molecular absorption, CIA from both H_2–H_2 and H_2–He, and Rayleigh scattering. We subsequently perform Bayesian spectral self-retrievals to retrieve for atmospheric metallicity and C/O ratio. Each retrieval is initiated with the parameters and priors listed below in Table 3, with atmospheric metallicity and C/O retaining the same initialization value and prior range for the full sample.

Results are obtained for all candidates in the *Twinkle* 7-yr candidate list, with the exception of K2-138 f, which is subsequently excluded from any analysis completed on the sample thereafter. We found persistent errors halting the retrieval of K2-138 f. While the exact cause of the error was not established, we note that K2-138 f has a very low mass, low gravity and an extremely high scale height of 1000 km, which could possibly be related to the computational failure.

We plot the results obtained, along with their 1σ error bars (mass from literature, metallicity from retrieval results) in Fig. 4, along with the injected mass–metallicity trend. In this figure, the central points are the medians of the posterior distributions and the errors bars encompass the 16th–84th percentile ranges. Although retrieved metallicity is found to be overestimated in all but four cases across the sample, this is a small effect, with 51/56 planets (91 per cent) of the population results having the truth value within the 1σ confidence interval.

This study indicates that *Twinkle* has the capability of recovering a mass–metallicity trend in cloud-free cool gaseous planet atmospheres. However, we acknowledge that some planets may have hazes and clouds. Also, our assumption of equilibrium chemistry is
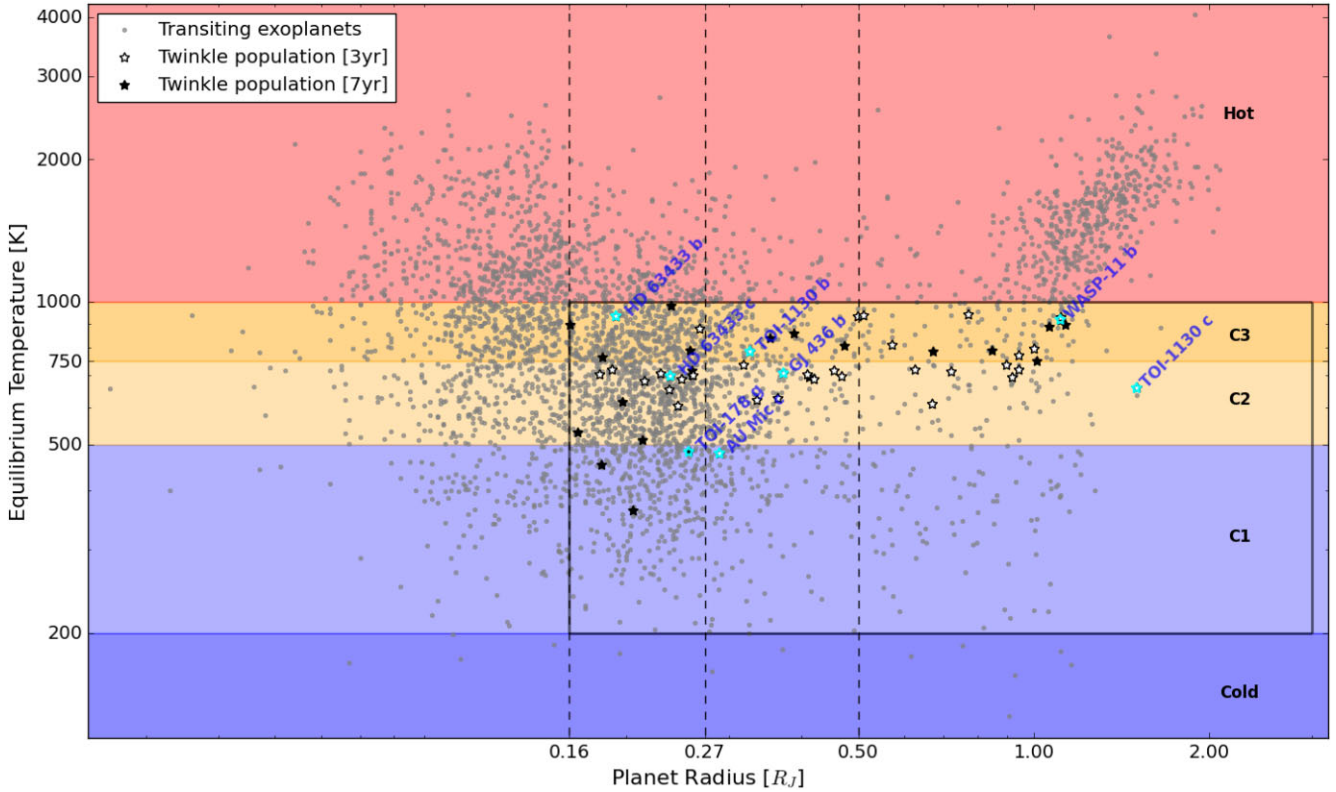
Figure 3. Population of known exoplanets [NASA Exoplanet Archive, accessed 23/05/18], overlain by candidates targeted by this study for the primary 3-yr and extended 7-year *Twinkle* exoplanet surveys. The different temperature regimes are indicated: Hot, C3, C2, C1, and cold. C1, C2, and C3 are three sub-categories of the 'cool' regime. The bounded region indicated the parameter space of cool gaseous planets as defined in this paper. The equilibrium temperatures shown for *Twinkle* 3- and 7-yr mission candidates are obtained from methodologies outlined in Edwards et al. (2019b) and used in the *TwinkleRad* data base. For all other planets, the equilibrium temperatures shown are obtained from the NASA archive where available or otherwise calculated from stellar and orbital parameters (assuming an albedo of 0.3).

Table 3. Initial values and prior ranges of free parameters in retrieval models used in the mass–metallicity study. Where factor bounds are used, values specified are multiplied by the truth value.

Parameter	Input	Prior type	Bounds
Metallicity, Z	50	Uniform, Linear	[0.01, 750]
C/O ratio	0.54	Uniform, Linear	[0.1, 5.0]
Radius	R_p	Uniform, Factor	[0.8 R_p, 1.2 R_p]
Temperature	T_{eq}	Uniform, Factor	[0.8 T_{eq}, 1.2 T_{eq}]

likely a simplification given the unknown nature of such atmospheres and the likelihood of disequilibrium processes. Further studies could therefore examine the robustness of recovering a mass–metallicity trend under a more complex variety of atmospheric scenarios, including a mix of cloudy, cloudless, and disequilibrium chemistry effects.

5.2 C/O ratio retrieval

In addition to retrieving for atmospheric metallicity, our study also retrieves for the carbon-to-oxygen ratio (C/O). Retrievals use the truth value as the input value in all cases, but implement a broad, uninformative prior as shown in Table 3. We find that the truth value is recovered within the 1σ confidence interval in all cases (as shown in the inset in Fig. 4). We do note that for 7 planets, the retrieved median values deviate strongly (by ≥0.135) from the injected truth,

with large error bars. We find that in the majority of these deviated cases, the posterior distributions were asymmetric with an extended positive tail, which may in part explain the overestimation given by the median.

5.3 Exploring sources of bias in metallicity retrievals

To explore the slight overestimation in retrieved metallicity seen for the bulk of the *Twinkle* 7 yr candidate population, we first explore the posterior distributions generated from the nested sampling retrieval results. Although there is some evidence of non-Gaussianity in the posterior distributions, as shown for TOI-1130 c in Fig. 5, we find no evidence for systematic overestimation of the median due to effects of sampling an asymmetric distribution.

We therefore elect to investigate the effect, if any, that the modelling and retrieval process has in creating this bias, by varying combinations of the wavelength grid and spectral resolution of the modelled spectra. This approach is taken as atmospheres are initially generated in TauREx using cross-sections that span the wavelength range 0.3–50 μm at a spectral resolution of $R = 15\,000$, resulting in a substantial loss of information from the model inputs when spectra are binned down to the specifications of the observing instrument. Three additional sets of models (Table 4, cases 2, 3, and 4) are generated using the wavelength ranges and spectral resolutions as listed, for each planet in the *Twinkle* 7-yr candidate list.

Here, case 1 is considered to be our baseline case, representing the performance of *Twinkle* based on current knowledge and modelling.
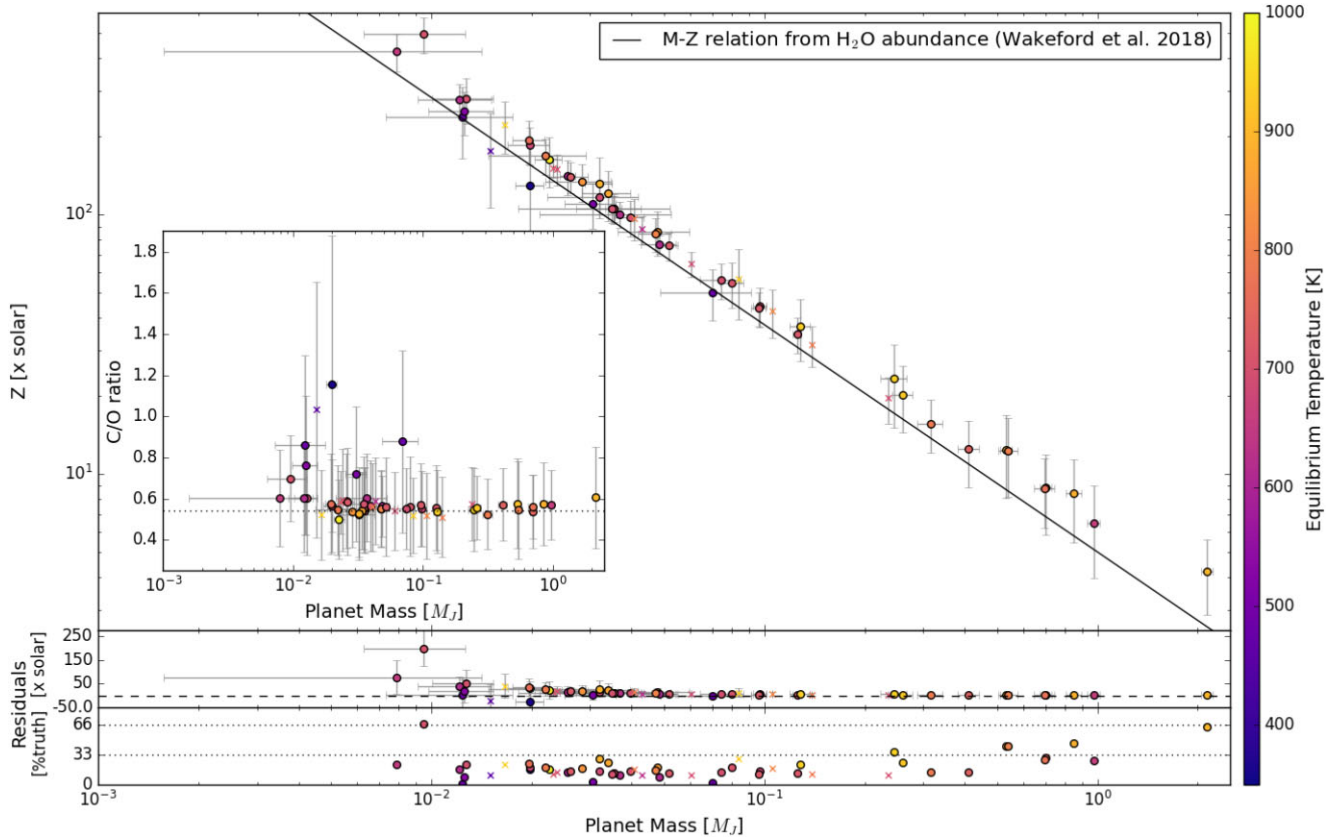
Figure 4. Retrieved metallicity plotted against literature mass. Inset shows retrieved C/O ratio against literature mass. Central points are the medians of the posterior distributions while error bars denoted the 1σ confidence interval (16th–84th percentile ranges). Here, we plot planets with currently measured masses as solid dots, whilst planets with masses estimated from M–R relations are plotted as crosses. Residuals with respect to input trend are shown in panel 2, whilst the residual normalized by the truth value is shown in panel 3.

Table 4. Metallicity bias study test cases.

Case number & name	Wavelength range	Wavelength grid
1 *Twinkle* native	0.5–4.5 μm	*Twinkle* native (average $R \sim 42$)
2 *Twinkle* - *HST* WFC3/G141 range	1.1–1.7 μm	*Twinkle* native (average $R \sim 44$)
3 *Twinkle* $R = 70$	0.5–4.5 μm	fixed $R = 70$
4 *Ariel* $R = 70$	0.5–7.8 μm	fixed $R = 70$

We base our case 2 model on the widely used *HST* WFC3/G141 instrument configuration to examine the effect of reducing the wavelength coverage compared to case 1 on retrieved metallicity, retaining the wavelength resolution grid of *Twinkle* such that any changes in retrieved metallicity can be attributed solely to the reduction in wavelength coverage. We use cases 3 and 4 to see the effect of increasing wavelength coverage from that of *Twinkle* to that of Ariel (approximately doubling the wavelength range). For consistency cases, 3 and 4 utilize a fixed R of 70. This R value does not reflect the true R for *Twinkle* or Ariel (which will vary with wavelength), but is chosen as a nominal value for the purposes of this comparison. Increased wavelength coverage would be expected to boost the sensitivity to of the retrieval to molecules such as CO (see Section 4.1). This approach is taken rather than accurately modelling an observation of these targets with *Ariel* due to the differences in native spectral resolution between *Twinkle* and *Ariel*, which would inhibit the ability to isolate the dependence on wavelength coverage on any systematic findings. We keep the error

bars on the spectra the same for each individual planet across all cases, and perform self-retrievals on the semi-physically motivated models of cases 2, 3, and 4 in the same manner described in Section 5.

Our findings are as follows: for case 2, average retrieved 1σ error ranges are just over a factor of 3 higher for atmospheric metallicity compared to case 1, yet despite this, values are typically found to be proportionately more overestimated, with only 35/56 planets (62.5 per cent of the population) having the truth value within the 1σ confidence interval. Comparisons between the baseline case (case 1) and case 3 show that the average retrieval error bars are comparable; the average 1σ confidence interval is 5 per cent greater in case 3 compared to case 1. The number of planets with truth values within the 1σ range is the same. Similar results are seen when comparing cases 3 and 4: in both cases, 51/56 planets have truth values within 1σ of the retrieved atmospheric metallicity values. However, the average retrieved 1σ range is 10 per cent smaller in case 4 compared to case 3.
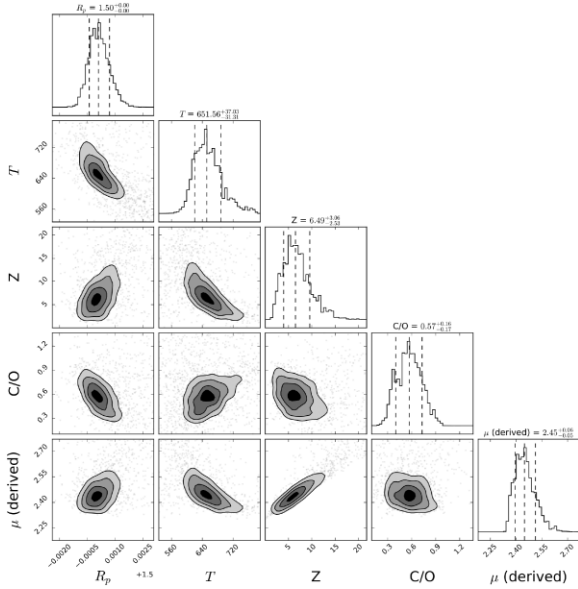
Figure 5. Retrieved joint posterior distribution for Tier 1 candidate TOI-1130 c.

Importantly, we find that in a little over two thirds of the sample (38/56 planets), case 4 spectra, with broader wavelength coverage, yield metallicity values that lie closer to the truth than in case 3. While this suggests that increased wavelength coverage leads to an improvement in the ability to recover atmospheric metallicity from spectra, further investigation shows that typically the absolute difference between retrieved metallicity and the truth value, $|Z_{ret}-Z_{truth}|$, is only marginally different between cases 3 and 4. We calculate this difference for each of the 56 planets in our sample using:

$$\delta = |Z_{ret} - Z_{truth}|_3 - |Z_{ret} - Z_{truth}|_4 \qquad (5)$$

The average value for δ is 1.3, which is well within the quadrature sum of the 1σ errors of the retrieved metallicities for each case (where the 1σ error is taken to be half of the 1σ confidence interval which is itself the 16th–84th percentile range). This suggests that the differences between cases 4 and 3 are not significant. We conclude that the slight bias seen in retrieved metallicity is likely at least in part due to information loss from reduced wavelength coverage, although other possible causes may exist.

6 CLOUD DETECTION STUDY

Clouds are thought to be present to some extent in the atmospheres of all planets (Helling 2021) and are known to make a significant contribution to the overall planetary albedo, a key parameter in the determination of equilibrium temperature (Estrela, Swain & Roudier 2022). Capable of influencing temperature, and hence the energy budget of an atmosphere, clouds are intrinsically coupled to T–P structure of the atmosphere and its chemical composition (Madhusudhan et al. 2016), with clouds of varying compositions expected to form as atmospheric species cross condensation fronts. Although the basic mechanisms by which cloud formation occurs are well-formulated, the precise details and balance of pathways are currently debated (Helling 2019, 2021). Consequently, the detection of clouds in cool gaseous planets and subsequent inference of the altitudes at which they are present, has the potential to provide

insight into atmospheric processes governing cloud formation in this regime.

We therefore investigate *Twinkle*'s capability to detect global cloud layers for a sub-sample of planets taken from the candidate list (Tables A1 and A2). We selected one representative planet from each of the nine major sub-divisions shown in Fig. 3 with the exception of C1-Jovian planets for which no examples exist in our list. The selected planets are indicated by name in Fig. 3.

Our goal here is to find constraints on the pressure levels at which cloudy atmospheres can be distinguished from cloud-free ones, functioning also as a top-level search for potential trends in cloud detectability across the different planetary types. Forward models are constructed using TauREx for each of the eight planets selected. Models are generated as previously described with isothermal profiles. ACE equilibrium chemistry is initiated with C/O = 0.54 (solar) and unique metallicity values for each planet from the H_2O mass–metallicity trend (including WASP-39 b) of Wakeford et al. (2018). The resulting altitude-dependent chemical profiles are then simplified to an individual altitude-independent VMR as described in Section 4.1 for H_2O, CH_4, CO_2, CO, NH_3, and N_2, and the model run again with fixed VMRs to generate the final transmission spectra. We include opacity contributions from molecules, Rayleigh scattering and CIA. In addition, an optically thick grey cloud layer is modelled at a given pressure level, which is varied between one of four pressures: 10^4, 10^3, 10^2, and 10 Pa in different runs. In each case, the resulting forward model spectra are then subjected to two Bayesian spectral retrievals. Both retrievals are conducted with identical initial input parameters and bounds, retrieving for all molecule VMRs, temperature, and planet radius, with one retrieval model retrieving for cloud pressure level, while the other does not include clouds.

Planetary radius and equilibrium temperature are fit with the same priors from Table 3, whilst log-uniform priors with bounds $[10^{-12}, 10^{-1}]$ are used for all molecule VMRs (H_2O, CH_4, CO_2, CO, NH_3, and N_2). Where clouds are included in the retrieval model, log-uniform priors with bounds $[10^{-6}, 10^5]$ Pa are used. We use the difference in the log Bayesian evidence from each pair of retrievals to determine a detection significance (Trotta 2008; Benneke & Seager 2013) for cloud (at the given pressure level) in each case. The results are illustrated in Fig. 6.

We find that high-altitude clouds at 10 Pa are detectable above 3σ irrespective of the planetary or temperature regime they are in. Deeper clouds at 100 Pa can be detected above 3σ across all planet sizes, but only in C2 and C3 (500–1000 K) planetary atmospheres.

At cloud pressure of 1000 Pa, we obtain 3σ detections only in the two Jovian planets, suggesting it may be possible to probe physical processes and T–P structure in the deeper layers down to 0.01 bar. At 10^4 Pa (0.1 bar), we are unable to distinguish cloudy and cloud-free atmospheres at $\geq 3\sigma$ in any of the cases.

These results indicate that *Twinkle* will be unlikely to detect clouds deeper than 0.1 bar in any cool gaseous planets, but that it should be able to detect clouds at 0.0001 bar (10 Pa) or higher across the full range of the cool gaseous planet regime. We find a rough indication of a trend of improved detectability with temperature and size of the planet. We also observe a tentative trend of decreasing sensitivity with planetary size across the sub-Neptune group and sub-Neptune–Neptune boundary; however, this may also be explicable by reduction in temperature in the lower detection planets. The robustness of these conclusions is limited due to the small sub-sample size used here. These initial results can be built on by further investigation using a larger sub-sample or a large grid of completely simulated planets (providing exact temperature and radius controls).
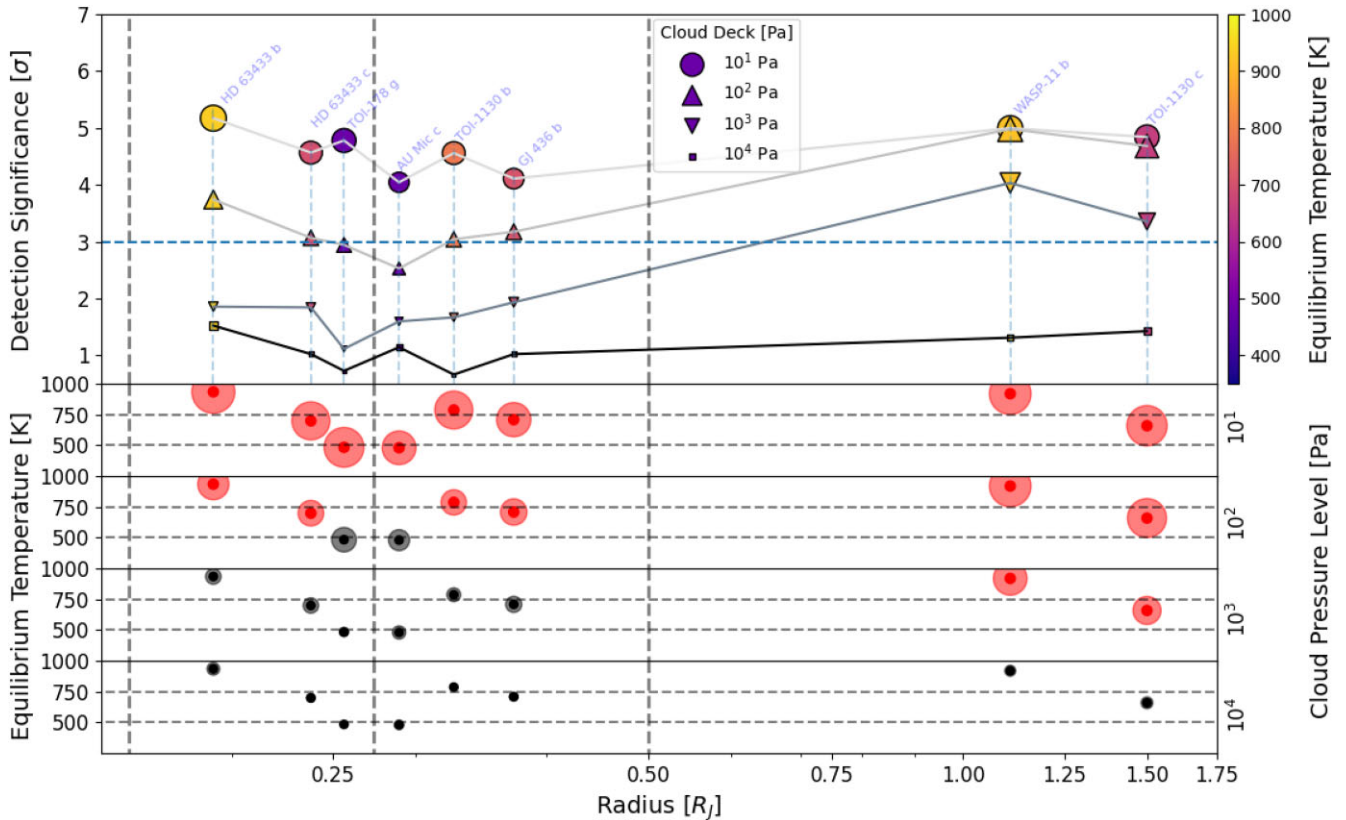
Figure 6. The upper plot shows statistical significance of cloud detection, derived from the Bayes factor preference for a model with clouds over model without clouds, for eight planets. The lower plot shows the temperature–radius plane for those eight planets with red circles indicating cases where detection significance is $>3\sigma$ while black circles denote cases at $<3\sigma$.

7 CONCLUSIONS

In summary, we present a first realization of a tiered candidate list for the proposed *Twinkle* cool gaseous planets survey, based on currently confirmed exoplanets. We find that *Twinkle* has the potential to characterize the atmospheres of up to 36 and 57 planets in the primary 3-yr and extended 7-yr survey, respectively. Candidates identified include 27 and 46 planets respectively that, to the best of the authors' knowledge at the time of submission, do not have precise transmission spectra. A survey using just Tier 1 and Tier 2 planets, would yield 20 planets ranging in mass from 0.0079 to 0.97 M_J and 480 to 941 K in temperature. Due to growing numbers of discoveries in the cool gaseous regime (e.g. by *TESS*) these sample sizes can be considered conservative and will be greater by the time of *Twinkle*'s launch. The final candidate list used for the *Twinkle* mission will be updated to include new discoveries.

Twinkle is well positioned to provide the first opportunity to garner insights into cool gaseous planets at a population level. The 3-yr baseline survey includes all 15 Tier 1 candidates (7 Jovians, 4 Neptunians, 4 sub-Neptunians, collectively spanning ∼480–934 K) and all 5 Tier 2 candidates. These planets will be the highest priority candidates for the survey. If planets up to Tier 3 are included, a 3-yr survey would have 31 planets, and a 7-yr survey would have 35 planets.

Our study predicts that major molecular species expected to be present under cloud-free near-equilibrium conditions in sub-1000 K atmospheres can be detected to high significance, and that if present, trends in atmospheric metallicity can be reliably identified across the sample of surveyed planets. The C/O ratio was also recovered

to within 1σ. These studies show that *Twinkle* will provide valuable data capable of contributing towards the understanding of trends within the cool gaseous planet demographic and beyond, as shown in Fig. 4. Such data have the potential to inform atmospheric models and further planet formation theories for giant planets in this understudied temperature regime.

We also predict that based on a simple grey cloud model, *Twinkle* has the potential to detect high-altitude cloud decks at or above 10 Pa in all atmospheric spectra in the cool regime, but would be insensitive to clouds below 10^4 Pa in all cases. We find a rough and tentative trend in cloud detectability with planetary temperature and size.

Cool gaseous planets represent a new frontier in exoplanet science, promising to expand our understanding of atmospheric physics and chemistry, as well as planet formation and evolution. The *Twinkle* cool gaseous planet survey has the potential to open up this uncharted territory of exoplanet parameter space with paradigm-shifting results. With 20 additional survey candidates present across tiers 2 and 3, and many new candidates, typically discovered around bright stars, hence amenable for transmission spectroscopy, confirmed and being actively refined by *TESS* and other facilities (including 32 new cool gaseous planets in the Twinkle field-of-regard), this proposed survey set to be conducted by *Twinkle* promises to deliver a small, but statistically meaningful sample of homogeneous spectra.

ACKNOWLEDGEMENTS

DATA AVAILABILITY

The data underlying this article will be shared on reasonable request to the corresponding author.

REFERENCES

Agúndez M., Martínez J. I., de Andres P. L., Cernicharo J., Martín-Gago J. A., 2020, A&A, 637, A59

Agúndez M., Venot O., Iro N., Selsis F., Hersant F., Hébrard E., Dobrijevic M., 2012, A&A, 548, A73

Al-Refaie A. F., Changeat Q., Waldmann I. P., Tinetti G., 2021, ApJ, 917, 37

Alam M. K. et al., 2022, ApJ, 927, L5

Alderson L. et al., 2023, Nature, 614, 664

Allart R. et al., 2023, A&A, 677, A164

Barclay T., Quintana E. V., Adams F. C., Ciardi D. R., Huber D., Foreman-Mackey D., Montet B. T., Caldwell D., 2015, ApJ, 809, 7

Baxter C. et al., 2021, A&A, 648, A127

Bell T. J. et al., 2023a, Nature, 623, 709

Benneke B. et al., 2019a, Nat. Astron., 3, 813

Benneke B. et al., 2019b, ApJ, 887, L14

Benneke B., Seager S., 2013, ApJ, 778, 153

Bézard B., Charnay B., Blain D., 2020, Nature Astronomy, 6, 537

Blain D., Charnay B., Bézard B., 2021, A&A, 646, A15

Boss A. P., 1997, Science, 276, 1836

Burn R., Schlecker M., Mordasini C., Emsenhuber A., Alibert Y., Henning T., Klahr H., Benz W., 2021, A&A, 656, A72

Charbonneau D., Brown T. M., Noyes R. W., Gilliland R. L., 2002, ApJ, 568, 377

Christiansen J. L. et al., 2022, AJ, 163, 244

Crossfield I. J. M., Kreidberg L., 2017, AJ, 154, 261

Drummond B. et al., 2020, A&A, 636, A68

Dymont A. H., Yu X., Ohno K., Zhang X., Fortney J. J., Thorngren D., Dickinson C., 2022, ApJ, 937, 90

Dyrek A. et al., 2023, Nature, 625, 51

Edwards B. et al., 2019a, Exp. Astron., 47, 29

Edwards B. et al., 2022, ApJS, 269, 46

Edwards B. et al., 2023, ApJ, 166, 26

Edwards B., Mugnai L., Tinetti G., Pascale E., Sarkar S., 2019b, AJ, 157, 242

Estrela R., Swain M. R., Roudier G. M., 2022, ApJ, 941, L5

Fleury B., Benilan Y., Venot O., Henderson B. L., Swain M., Gudipati M. S., 2023, ApJ, 956, 134

Fortney J. J., Visscher C., Marley M. S., Hood C. E., Line M. R., Thorngren D. P., Freedman R. S., Lupu R., 2020, AJ, 160, 288

Fulton B. J. et al., 2017, AJ, 154, 109

Gao P. et al., 2023, ApJ, 951, 96

Garai Z. et al., 2023, A&A, 674, 14

Gillon M. et al., 2017, Nature, 542, 456

Greaves J. S. et al., 2021, Nat. Astron., 5, 655

Guilluy G. et al., 2021, AJ, 161, 19

Gupta A., Schlichting H. E., 2019, MNRAS, 487, 24

Han T. et al., 2023, ApJ, 167, 14

Harris M. et al., 2023, ApJ, 959, 14

Hawthorn F. et al., 2023, MNRAS, 528, 1841

Heller R., Pudritz R., 2015, ApJ, 806, 181

Helling C., 2019, Annu. Rev. Earth Planet Sci., 47, 583

Helling C., 2021, in Madhusudhan N., ed., ExoFrontiers; Big Questions in Exoplanetary Science. IOP, p. 20

Hill M. L., Kane S. R., Seperuelo Duarte E., Kopparapu R. K., Gelino D. M., Wittenmyer R. A., 2018, ApJ, 860, 67

Hobson M. J. et al., 2023, AJ, 166, 201

Hu R., Seager S., Yung Y. L., 2015, ApJ, 807, 8

Ida S., Lin D. N. C., 2005, ApJ, 626, 1045

Kammer J. A. et al., 2015, ApJ, 810, 118

Kanodia S. et al., 2023, AJ, 165, 120

Kempton E. M. R. et al., 2023, Nature, 620, 67

Kipping D., Yahalomi D. A., 2023, MNRAS, 518, 3482

Knierim H., Shibata S., Helled R., 2022, A&A, 665, L5

Knutson H. A. et al., 2014b, ApJ, 794, 155

Knutson H. A., Benneke B., Deming D., Homeier D., 2014a, Nature, 505, 66

Kreidberg L., 2014, Nature, 505, 69

Kreidberg L. et al., 2022, AJ, 164, 124

Kreidberg L., Line M. R., Thorngren D., Morley C. V., Stevenson K. B., 2018, ApJ, 858, L6

Libby-Roberts J. E. et al., 2020, AJ, 159, 57

Lingam M., Loeb A., 2019, ApJ, 883, 143

Lissauer J. J., Dawson R. I., Tremaine S., 2014, Nature, 513, 336

Madhusudhan N., 2012, ApJ, 758, 36

Madhusudhan N., Agúndez M., Moses J. I., Hu Y., 2016, Space Sci. Rev., 205, 285

Madhusudhan N., Piette A. A. A., Constantinou S., 2021, ApJ, 918, 1

Madhusudhan N., Sarkar S., Constantinou S., Holmberg M., Piette A. A. A., Moses J. I., 2023, ApJ, 956, L16

Mayor M., Queloz D., 1995, Nature, 378, 355

Mazeh T., Holczer T., Faigler S., 2016, A&A, 589, A75

McGruder C. D., López-Morales M., Brahm R., Jordán A., 2023, ApJ, 944, L56

Mikal-Evans T. et al., 2023, AJ, 165, 84

Mireles I. et al., 2023, ApJ, 954, L15

Moses J. I. et al., 2011, ApJ, 737, 15

Moses J. I., 2014, Phil. Trans. R. Soc. A, 372, 20130073

Mugnai L. V., Pascale E., Edwards B., Papageorgiou A., Sarkar S., 2022, JOSS, 8, 5348

Öberg K. I., Murray-Clay R., Bergin E. A., 2011, ApJ, 743, L16

Osborn H. P. et al., 2023, MNRAS, 523, 3069

Paardekooper S.-J., Johansen A., 2018, Space Sci. Rev., 214, 38

Pacetti E. et al., 2022, ApJ, 937, 36

Pollack J. B., Hubickyj O., Bodenheimer P., Lissauer J. J., Podolak M., Greenzweig Y., 1996, Icarus, 124, 62

Powers L. C. et al., 2023, AJ, 166, 44

Prinn R. G., Barshay S. S., 1977, Science, 198, 1031

Rovira-Navarro M., van der Wal W., Steinke T., Dirkx D., 2021, Planet. Sci. J., 2, 119

Roy P.-A. et al., 2023, ApJ, 954, L52

Rustamkulov Z. et al., 2023, Nature, 614, 659

Sagan C., Salpeter E. E., 1976, ApJS, 32, 737

Saillenfest M., Sulis S., Charpentier P., Santerne A., 2023, A&A, 675, 15

Seager S., Petkowski J. J., Günther M. N., Bains W., Mikal-Evans T., Deming D., 2021, Universe, 7, 172

Sing D. K. et al., 2016, Nature, 529, 59

Spake J. J., Oklopčić A., Hillenbrand L. A., 2021, AJ, 162, 284

Spalding C., Batygin K., Adams F. C., 2016, ApJ, 817, 18

Stotesbury I. et al., 2022, in Coyle L. E., Matsuura S., Perrin M. D., eds, Proc. SPIE Conf. Ser. Vol. 12180, Space Telescopes and Instrumentation 2022: Optical, Infrared, and Millimeter Wave. SPIE, Bellingham, p. 1218033

Sucerquia M., Ramírez V., Alvarado-Montes J. A., Zuluaga J. I., 2020, MNRAS, 492, 3499

Swift J. J., Johnson J. A., Morton T. D., Crepp J. R., Montet B. T., Fabrycky D. C., Muirhead P. S., 2013, ApJ, 764, 105

Szabó G. M., Kiss L. L., 2011, ApJ, 727, L44

Tennyson J., Yurchenko S. N., 2016, Int. J. Quantum Chem., 117, 92

Thao P. C. et al., 2023, AJ, 165, 23

Thorngren D. P., Fortney J. J., Murray-Clay R. A., Lopez E. D., 2016, ApJ, 831, 64

Thorngren D. P., Marley M. S., Fortney J. J., 2019, Res. Notes Am. Astron. Soc., 3, 128

Tinetti G., Drossart P., Eccleston P. et al., 2018, Exp. Astron., 46, 135
Trotta R., 2008, Contemporary Physics, 49, 71
Tsai S.-M. et al., 2023, Nature, 617, 483
Tsai S.-M., Lyons J. R., Grosheintz L., Rimmer P. B., Kitzmann D., Heng K., 2017, ApJS, 228, 20
Tsiaras A. et al., 2018, AJ, 155, 156
Tsiaras A., Waldmann I. P., Tinetti G., Tennyson J., Yurchenko S. N., 2019, Nat. Astrono., 3, 1086
Turrini D. et al., 2021, ApJ, 909, 40
Tuson A. et al., 2023, MNRAS, 523, 3090
Ulmer-Moll S. et al., 2023, A&A, 674, A43
Vissapragada S. et al., 2022, AJ, 164, 234
Wakeford H. R. et al., 2018, AJ, 155, 29
Waldmann I. P., Tinetti G., Rocchetto M., Barton E. J., Yurchenko S. N., Tennyson J., 2015, ApJ, 802, 107
Wallack N. L. et al., 2019, AJ, 158, 217
Welbanks L., Madhusudhan N., Allard N. F., Hubeny I., Spiegelman F., Leininger T., 2019, ApJ, 887, L20
Wittenmyer R. A. et al., 2020, MNRAS, 492, 377
Wolszczan A., 2012, New Astron. Rev., 56, 2
Wong I. et al., 2022, AJ, 164, 30
Yates J. S., Palmer P. I., Biller B., Cockell C. S., 2017, ApJ, 836, 184
Yoshida S. et al., 2023, AJ, 166, 181
Zahnle K. J., Marley M. S., 2014, ApJ, 797, 41
Zamyatina M. et al., 2023, MNRAS, 519, 3129
Zhang X., 2020, Res. Astron. Astrophys., 20, 099

APPENDIX A: CANDIDATE LISTS

Table A1. Candidate planets in Tiers 1, 2, and 3 for the *Twinkle* cool gaseous planet survey. Planetary and stellar parameters listed are used throughout this work and were obtained from the NASA Exoplanet Archive or calculated based on assumptions presented in Edwards et al. (2019b). Where unavailable in the archive, host star spectral type uses SIMBAD values ([‡]) or estimation based on comparable stars ([†]).

Planet name	N_t	T_{int} [d]	R_p [R_J]	M_p [M_J]	T_{eq} [K]	In 3 yr List	In 7 yr List	Tier	Transmission Spectra	R_s [$R_\odot$]	T_s [K]	Spectral Type
AU Mic b	2	0.904	0.363	$0.0368^{+0.0157}_{-0.0157}$	626.428	Y	Y	1	False	0.75	3700	M1
AU Mic c	20	11.359	0.289	$0.0699^{+0.0211}_{-0.0211}$	479.593	Y	Y	1	False	0.75	3700	M1
GJ 1214 b	15	1.581	0.245	$0.0257^{+0.0014}_{-0.0014}$	603.949	Y	Y	1	True	0.21	3250	M4
GJ 3470 b	7	1.602	0.408	$0.0396^{+0.0040}_{-0.0040}$	702.732	Y	Y	1	True	0.55	3600	M1.5
GJ 436 b	4	0.590	0.372	$0.0799^{+0.0066}_{-0.0063}$	708.023	Y	Y	1	True	0.46	3586	M2.5
HD 136352 c	17	6.975	0.260	$0.0354^{+0.0021}_{-0.0020}$	701.029	Y	Y	1	False	1.06	5564	G4
HD 63433 b	20	8.014	0.192	0.0166	934.262	Y	Y	1	False	0.91	5640	G5
HD 63433 c	17	8.584	0.238	0.0239	698.391	Y	Y	1	False	0.91	5640	G5
K2-141 c	1	0.333	0.624	0.0233	720.185	Y	Y	1	False	0.68	4599	K7
K2-24 c	22	19.008	0.669	$0.0485^{+0.0060}_{-0.0057}$	610.027	Y	Y	1	False	1.16	5625	G9
TOI-1130 c	8	2.056	1.500	$0.9740^{+0.0430}_{-0.0440}$	658.620	Y	Y	1	False	0.69	4250	K7
V1298 Tau b	22	18.094	0.916	0.2360	695.412	Y	Y	1	False	1.34	4970	K0
WASP-107 b	1	0.351	0.940	$0.0960^{+0.0050}_{-0.0050}$	719.812	Y	Y	1	True	0.67	4425	K6
WASP-69 b	2	0.556	1.110	$0.2600^{+0.0185}_{-0.0185}$	928.605	Y	Y	1	True	0.86	4700	K5
WASP-80 b	10	2.695	0.999	$0.5400^{+0.0360}_{-0.0350}$	799.369	Y	Y	1	True	0.59	4143	K7-M0
HD 183579 b	42	23.804	0.317	$0.0352^{+0.0170}_{-0.0170}$	736.129	Y	Y	2	False	0.99	5788	G2
TOI-1064 c	36	10.697	0.237	$0.0079^{+0.0063}_{-0.0057}$	653.762	Y	Y	2	False	0.73	4734	K3-K5[†]
TOI-178 d	46	13.424	0.229	$0.0095^{+0.0025}_{-0.0032}$	708.942	Y	Y	2	False	0.65	4316	K7[†]
TOI-421 c	27	10.674	0.454	$0.0517^{+0.0033}_{-0.0033}$	717.787	Y	Y	2	False	0.87	5325	G7
WASP-29 b	29	9.770	0.770	$0.2450^{+0.0230}_{-0.0220}$	941.816	Y	Y	2	True	0.79	4800	K4[‡]
GJ 9827 d	79	12.006	0.180	$0.0127^{+0.0026}_{-0.0026}$	705.214	Y	Y	3	False	0.60	4340	K6
HATS-72 b	57	21.946	0.722	$0.1254^{+0.0039}_{-0.0039}$	714.490	Y	Y	3	False	0.72	4656	K5[†]
HD 106315 c	96	67.606	0.388	$0.0478^{+0.0116}_{-0.0116}$	858.332	N	Y	3	False	1.30	6327	F5
HD 63935 b	71	29.872	0.267	$0.0340^{+0.0057}_{-0.0057}$	877.525	Y	Y	3	False	0.96	5534	G5[‡]
HD 63935 c	97	59.066	0.259	$0.0349^{+0.0076}_{-0.0076}$	701.589	N	Y	3	False	0.96	5534	G5[‡]
HD 73583 b	54	14.314	0.249	$0.0321^{+0.0107}_{-0.0098}$	688.149	Y	Y	3	False	0.65	4511	K4
HD 97658 b	62	21.795	0.189	$0.0261^{+0.0035}_{-0.0035}$	720.334	Y	Y	3	True	0.73	5212	K1
K2-406 b	71	41.930	0.411	0.0603	693.947	N	Y	3	False	0.96	5784	G4
TOI-1130 b	83	21.998	0.326	0.0407	786.160	Y	Y	3	False	0.69	4250	K7
TOI-178 g	94	25.339	0.256	$0.0124^{+0.0041}_{-0.0051}$	483.212	N	Y	3	False	0.65	4316	K7[†]
TOI-620 b	61	9.190	0.335	0.0428	620.967	Y	Y	3	False	0.55	3708	M2.5
TOI-674 b	68	10.035	0.468	$0.0743^{+0.0104}_{-0.0104}$	698.867	Y	Y	3	False	0.42	3514	M2
V1298 Tau c	83	48.488	0.499	0.0839	932.639	Y	Y	3	False	1.34	4962	K0
V1298 Tau d	65	44.450	0.572	0.1060	814.103	Y	Y	3	False	1.34	4962	K0
WASP-11 b	57	17.901	1.110	$0.5320^{+0.0210}_{-0.0200}$	918.615	Y	Y	3	False	0.89	4800	K3

Table A2. Candidate planets in Tiers 4 and 5 for the *Twinkle* cool gaseous planet survey. Planetary and stellar parameters listed are used throughout this work and were obtained from the NASA Exoplanet Archive or calculated based on assumptions presented in Edwards et al. (2019b). Where unavailable in the archive, host star spectral type uses SIMBAD values ($\ddagger$) or estimation based on comparable stars ($\dagger$).

Planet name	N_t	T_{int} [d]	R_p [R_J]	M_p [M_J]	T_{eq} [K]	In 3 yr List	In 7 yr List	Tier	Transmission Spectra	R_s [$R_\odot$]	T_s [K]	Spectral Type
HD 73583 c	136	60.023	0.213	$0.0305^{+0.0057}_{-0.0054}$	510.880	N	Y	4	False	0.65	4511	K4
K2-287 b	143	80.315	0.847	$0.3150^{+0.0270}_{-0.0270}$	790.363	N	Y	4	False	1.07	5695	G8
K2-32 b	126	54.426	0.473	$0.0472^{+0.0057}_{-0.0054}$	808.226	N	Y	4	False	0.86	5271	G9
LP 714-47 b	143	27.265	0.419	$0.0969^{+0.0047}_{-0.0047}$	686.753	Y	Y	4	False	0.58	3950	M0
TOI-561 c	142	66.441	0.257	$0.0220^{+0.0072}_{-0.0072}$	789.277	N	Y	4	False	0.85	5455	G9
TOI-776 b	140	42.583	0.165	$0.0126^{+0.0028}_{-0.0028}$	530.605	N	Y	4	False	0.54	3709	M1
WASP-132 b	134	53.011	0.897	$0.4100^{+0.0300}_{-0.0300}$	736.759	Y	Y	4	False	0.75	4714	K4
WASP-84 b	123	42.392	0.942	$0.6940^{+0.0490}_{-0.0470}$	773.076	Y	Y	4	False	0.75	5314	K0
G 9-40 b	375	58.498	0.181	0.0150	454.032	N	Y	5	False	0.31	3348	M2.5
K2-121 b	309	96.569	0.671	0.1390	786.419	N	Y	5	False	0.67	4690	K5‡
K2-138 f	181	72.914	0.259	$0.0051^{+0.0067}_{-0.0037}$	715.911	N	Y	5	False	0.86	5356	G8
LTT 3780 c	174	38.081	0.204	$0.0198^{+0.0020}_{-0.0019}$	363.418	N	Y	5	False	0.37	3331	M4
TOI-1201 b	234	44.232	0.215	$0.0198^{+0.0026}_{-0.0028}$	682.774	Y	Y	5	False	0.51	3476	M2
TOI-1422 b	173	96.480	0.353	$0.0283^{+0.0072}_{-0.0063}$	838.973	N	Y	5	False	1.02	5840	G2
TOI-1478 b	208	108.544	1.060	$0.8510^{+0.0520}_{-0.0470}$	889.609	N	Y	5	False	1.05	5597	G8
TOI-1634 b	1888	244.729	0.160	$0.0319^{+0.0030}_{-0.0030}$	894.156	N	Y	5	False	0.45	3550	M2
TOI-178 e	231	71.965	0.197	$0.0121^{+0.0039}_{-0.0030}$	616.710	N	Y	5	False	0.65	4316	K7†
TOI-3714 b	693	150.617	1.010	$0.7000^{+0.0300}_{-0.0300}$	749.785	N	Y	5	False	0.51	3660	M2
TOI-421 b	322	50.217	0.239	$0.0226^{+0.0021}_{-0.0021}$	982.024	N	Y	5	False	0.87	5325	G9
WASP-156 b	280	84.476	0.510	$0.1280^{+0.0100}_{-0.0090}$	938.278	Y	Y	5	False	0.76	4910	K3
WASP-8 b	236	94.124	1.130	$2.1320^{+0.0800}_{-0.0810}$	896.199	N	Y	5	False	1.03	5600	G8
Wolf 503 b	271	69.390	0.182	$0.0197^{+0.0022}_{-0.0022}$	764.360	N	Y	5	False	0.69	4716	K3.5

This paper has been typeset from a TEX/LATEX file prepared by the author.